Contents lists available at ScienceDirect

Materials Today Communications

Morphological transformations mapping of CaXO$_4$ (X = Mo or W) and their surface stability

José A.S. Laranjeira [a], Guilherme S.L. Fabris [b], Anderson R. Albuquerque [c], Mateus M. Ferrer [d], Julio R. Sambrano [a,*]

[a] *Modeling and Molecular Simulation Group, Sao Paulo State University Julio de Mesquita Filho, Bauru, SP, Brazil*
[b] *Department of Materials Engineering, Federal University of Rio Grande do Norte, 59078-970 Natal, Brazil*
[c] *Chemistry Institute, Federal University of Rio Grande do Norte, 59078-970 Natal, RN, Brazil*
[d] *Technological Development Center, Federal University of Pelotas, 96010-610 Pelotas, RS, Brazil*

ARTICLE INFO

ABSTRACT

The knowledge about the mechanisms of the morphological control of nanoparticles (NPs) is directly correlated with the atomic configurations of their exposed surfaces, which can facilitate materials functionalization according to the surface-dependent properties. In this context, this study focused on modeling via the density functional theory (DFT) the (001), (100), (101), (103), (110), (111), and (112) surfaces of the CaXO$_4$ (X = Mo or W) (scheelite phase) to offer a comprehensive study of their structural and electronic properties. Additionally, a systematic mapping of the NPs morphology was elaborated as a function of the modulation of the surface energies. For the surfaces of both systems, a stability order of (001) > (112) > (111) > (101) > (110) > (103) > (100) was observed. Differences were observed in both systems concerning the outermost polyhedral distortion and their atomic charges. The band alignment analysis revealed the potential use of both materials in photocatalytic environmental remediation. The methodology and results presented herein can be useful for targeting the synthesis and functionalization of CaXO4 and related materials.

1. Introduction

The control of nanoparticle (NP) morphology has received much attention in recent years due to its influence on the properties of the materials [1–4]. The morphology control depends on several parameters, such as reaction time, temperature, pressure, surfactants, and pH, and can be adjusted according to several synthesis methods [3,5–9]. In this context, theoretical research has been dedicated to studying special features of NPs, including the atomic configuration of their exposed surfaces and their respective electronic properties [10–20]. In particular, the NP morphology is directly connected with the surface energy of their facets by an inversely proportional relation, where the lower the surface energy is, the greater their exposed area. However, the experimental determination of surface energies at the nanoscale is still a challenge for experimentalists. In this sense, theoretical methods have been used to estimate these values. According to the classical Wulff theory [21], the crystal equilibrium shape is determined by minimizing the total surface energy for a given volume.

In this study, the particular interest is in the molybdate and tungstate

families, which have been applied in optical fibers, [22], scintillators, [23,24], multiferroic materials, [25,26], humidity sensors, [27,28], high-temperature lubricants, [29], corrosion inhibitors, [30,31], battery materials, [32], antenna materials [33] and catalysts [34,35]. Among these compounds, calcium molybdate (CaMoO$_4$) and calcium tungstate (CaWO$_4$), both scheelite-type ABO$_4$ (A = Cd, Ca, Sr, Pb or Ba and B = Mo or W), have interesting thermal and luminescent properties and can be applied in phosphors, scintillators, optical fibers and gas sensors [36,37] or used as hosts for components emitting green color in white LEDs [38].

CaXO$_4$ (X = Mo or W) compounds have been the focus of theoretical and experimental studies evaluating the effects of their morphological transformations [2,39–41]. In particular, Longo et al. [42] synthesized CaWO$_4$ NPs with octahedron with flattened tips morphology via the microwave-assisted hydrothermal method. In addition, the relative stability and electronic properties of the surfaces were also calculated, resulting in the following stability order: (001) > (101) > (100) > (110) > (103) > (111). In contrast, Oliveira et al. [40] obtained dodecahedron-shaped CaMoO4 NPs by MAH and calculated the stability order (001) > (112) > (110) > (101) > (100) > (111). The authors

---

* Corresponding author.
  E-mail address: jr.sambrano@unesp.br (J.R. Sambrano).

proposed surface energy stabilization routes from these theoretical results representing the experimental nanoparticle shapes achieved. Comparing these two studies, it is possible to observe differences in the relative stability order and two different terminations of the (101) surface. Longo et al. [42] reported that such a surface is terminated in [CaO_5] polyhedra, while Oliveira et al. [40] found the termination of [MoO_4] polyhedra.

In this sense, it is important to highlight that the success of surface simulations depends directly on the knowledge of the most stable atomic configurations of the outermost layers [4,43–45]. Therefore, considering the differences observed in the abovementioned studies, it is noteworthy that a consensus regarding the atomic configuration of the outermost layers of the exposed NP facets and their stability order is crucial for the success and accuracy of the simulation results. Therefore, it is possible to modulate the electronic characteristics and their technological applications [46–48].

Due to the direct correlation between the surface-dependent properties and morphology of NPs [49–54], this study aimed to carry out computational simulations based on density functional theory (DFT) [55] to evaluate the electronic and structural properties as well as the relative stability of the (001), (100), (101), (103), (110), (111) and (112) surfaces of $CaXO_4$ (X = Mo or W). The selection of surfaces was made according to the Bravais-Friedel-Donnay-Harker law [56–58] which states that the most important facets are those with greater interplanar distances due to space-group symmetry. The results of the relative stability of the surfaces were used to generate the ideal NP morphology and elaborate a complete mapping of the morphological transformations of their NPs. Additionally, the densities of states of the NPs were simulated, considering the surface contributions.

2. Computational procedure

The simulations were performed using the periodic DFT methodology implemented in the CRYSTAL17 program [59]. The atomic centers of Ca, Mo, W, and O were described by the triple-zeta valence with polarization (TZVP) [60], Hay-Wadt-311(d31)G, [61], cora_1996 [62] and 8–411d1 [63] basis sets, respectively.

Initially, both $CaMoO_4$ and $CaWO_4$ bulk structures were optimized, starting from the respective experimental lattice parameters. Both systems have a scheelite-type structure and belong to the space group I41/a (symmetry C_{4h}^6) and lattice parameters a = b = 5.233 Å and c = 11.448 Å for $CaMoO_4$ and a = b = 5.243 Å and c = 11.376 Å for $CaWO_4$, which are formed by [CaO_8] and [MoO_4] (or [WO_4]) polyhedra [64]. Fig. 1 depicts the respective structures.

It is known that the crucial point to designing accurate models via DFT formalism is the choice of the functional to be used in the target systems. For this reason, several tests were made in the set of the following seven hybrid density functionals: B1WC [65], B3LYP [66], HSE06 [67,68], PBE0 [69] and WC1LYP [70]. Compared to the experimental parameters for both systems, the B1WC was the functional that provided the best results for lattice parameters and band gap energy (E_{gap}) for the $CaXO_4$ compounds (see Table 1). The equation that defines the B1WC functional is $E_{XC}^{B1WC} = E_X^{GGA} + P(E_X^{HF} - E_X^{GGA})$, where E_X^{GGA} is the GGA exchange energy, E_X^{HF} is the Hartree–Fock (HF) exchange energy, and $P = 16\%$ is the HF exchange parameter. By adopting the same methodology reported by Gomes et al. [71], a scan of the P parameter was performed in the range from 10% to 20%, where $P = 13.2\%$ showed better accuracy.

Table 1 lists the percentage differences from the experimental parameters of the B1WC functional, showing the lattice parameters and E_{gap} (before and after the P parameter scan). Although there was no considerable change in the approximation to the lattice parameters, there was a significant improvement in the E_{gap} accuracy, from 11.1% to 6.5% for $CaMoO_4$ and from 7.2% to 1.4% for $CaWO_4$.

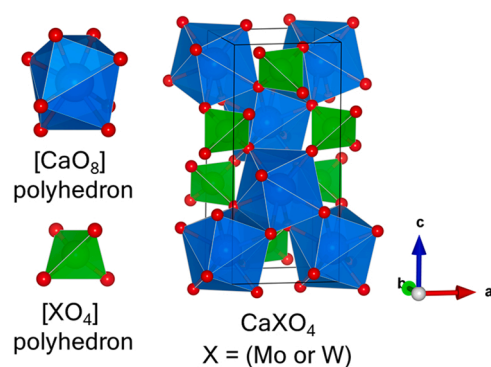To better understand the structural behavior of both systems in an

Fig. 1. The unit cell of $CaXO_4$ (X = Mo or W) and octahedral [CaO_8] and tetragonal [XO_4] (X = Mo or W) polyhedra are highlighted.

equilibrium state, the NP morphology was determined using the classical Wulff's theory [4,21] and the calculated surface energies (E_{surf}), whose general formula is defined by $E_{surf} = (E_{model} - nE_{bulk})/2A$, where E_{model} is the total energy of the surface model, E_{bulk} is the total energy of the bulk, n is the number of bulk units in the surface model, and A is the unit cell surface area. The (001), (100), (101), (103), (110), (111), and (112) surfaces were analyzed using models that have reached the E_{surf} convergence ($\Delta E_{surf}(z) < 0.01 J/m^2$) with the stoichiometric increases of atomic layers in the z-direction. A morphological network diagram was elaborated from a combination of surface energies of the exposed surfaces according to the methodology used by Laranjeira et al. [4].

The parameters described below were used in all simulations. The precision of the infinite Coulomb and HF exchange series is controlled by five parameters α_i, with i = 1, 2, 3, 4, and 5, where α_1 is the overlap, and α_2 is the penetration for Coulomb integrals, α_3 is the overlap for HF exchange integrals and α_4 and α_5 are the pseudo-overlap (HF exchange series). The five parameters α_i were set to 8, 8, 8, 8, and 16, respectively. The two-electron contributions are neglected when the overlap between atomic functions is below $10^{-\alpha_i}$. The convergence criteria for the electronic energy were set to 10^{-6} u.a. For periodic systems, the only mandatory parameter is the shrinking factor, which generates a proportional grid of k-points in reciprocal space, according to the

Table 1

Lattice parameters ($a = b$ and c) (Å) and band gap energy (E_{gap}) (eV) for $CaXO_4$ within the B1WC (13.2%) functional. The values in parentheses indicate the percentage differences compared to the experimental data.

	Functional	$a = b$	c	E_{gap}
$CaMoO_4$	B1WC	5.23 (0.0%)	11.29 (1.4%)	4.62 (11.1%)
	B1WC (13.2%)	5.29 (1.1%)	11.48 (0.3%)	4.43 (6.5%)
	Exp.[64,72]	5.23	11.45	4.16
$CaWO_4$	B1WC	5.26 (0.3%)	11.50 (1.1%)	5.21 (7.2%)
	B1WC (13.2%)	5.26 (0.3%)	11.51 (1.1%)	4.93 (1.4%)
	Exp.[72,73]	5.243	11.376	4.86

Table 2

Hirshfeld atomic charges (q) in elementary charge units (|e|) for the bulk and outermost atoms of the $CaXO_4$ surfaces.

	$CaMoO_4$			$CaWO_4$		
Charge	Ca	Mo	O	Ca	W	O
Bulk	2.067	1.322	-1.108	2.118	3.151	-1.317
(001)	2.038	2.288	-0.946	2.081	3.080	-1.152
(112)	2.054	2.310	-0.677	2.098	3.079	-0.888
(111)	2.041	2.266	-0.708	2.083	3.057	-0.918
(101)	2.032	2.327	-1.009	2.078	3.111	-1.216
(110)	2.035	2.252	-0.710	2.076	3.038	-0.918
(103)	2.030	2.181	-1.118	2.071	2.995	-1.318
(100)	2.049	2.294	-0.677	2.095	3.081	-0.884

Monkhorst-Pack method. The reciprocal space integration used was an $8 \times 8 \times 8$ k-point mesh (8 x 8 x 1 for surface models) in the irreducible Brillouin zone. The geometry optimization calculations demonstrate that the optimized structures are in agreement with the space group symmetry for both materials.

3. Results and discussion

Fig. 2 shows a side view, the outermost polyhedra, and a top view of their respective electrostatic potential surfaces of the most stable terminations of the (001), (112), (111), (101), (110), (103), and (100)
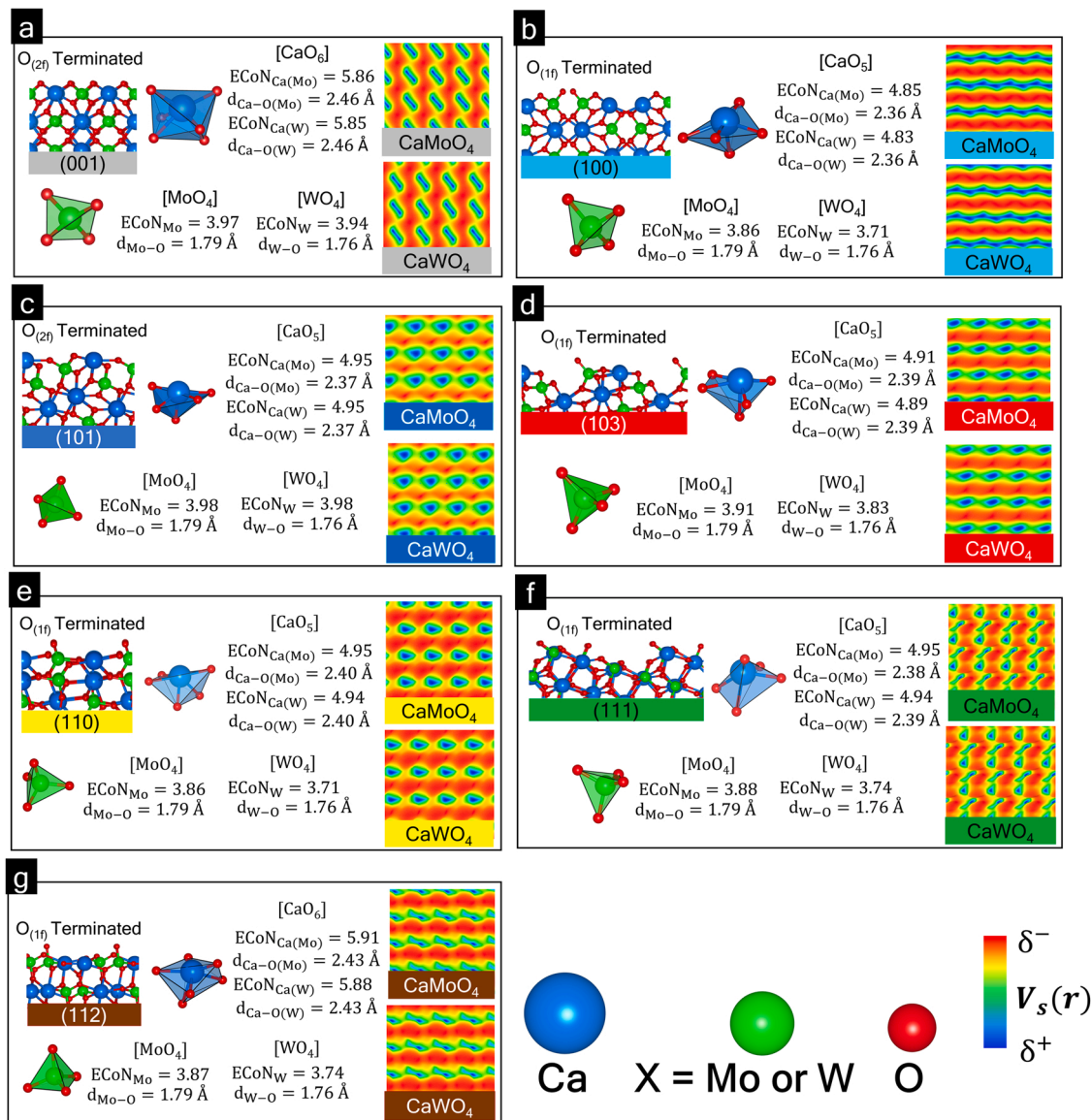

Fig. 2. Side view of the outermost layers of CaXO$_4$ surfaces, effective coordination number (ECoN$_{Ca(Mo\ or\ W)}$ and ECoN$_{(Mo\ or\ W)}$), average bond length (d$_{Ca-O(Mo\ or\ W)}$ and d$_{(Mo\ or\ W)-O}$) for the outermost Ca (Mo or W), Mo (or W)-centered polyhedra, respectively, and electrostatic surface potentials (V$_s$(r)) top view for (a) (001), (b) (100), (c) (110), (d) (112), (e) (101), (f) (103), and (g) (111) surfaces), where Mo and W refer to CaMoO$_4$ and CaWO$_4$-based systems, respectively.

Table 3

Surface energy after (E_{surf}) (J/m^2) and before ($E_{surf}^{non-opt}$) (J/m^2) optimization, model thickness (L) (Å), and band gap energy (E_{gap}) (eV) for CaXO$_4$ surface models.

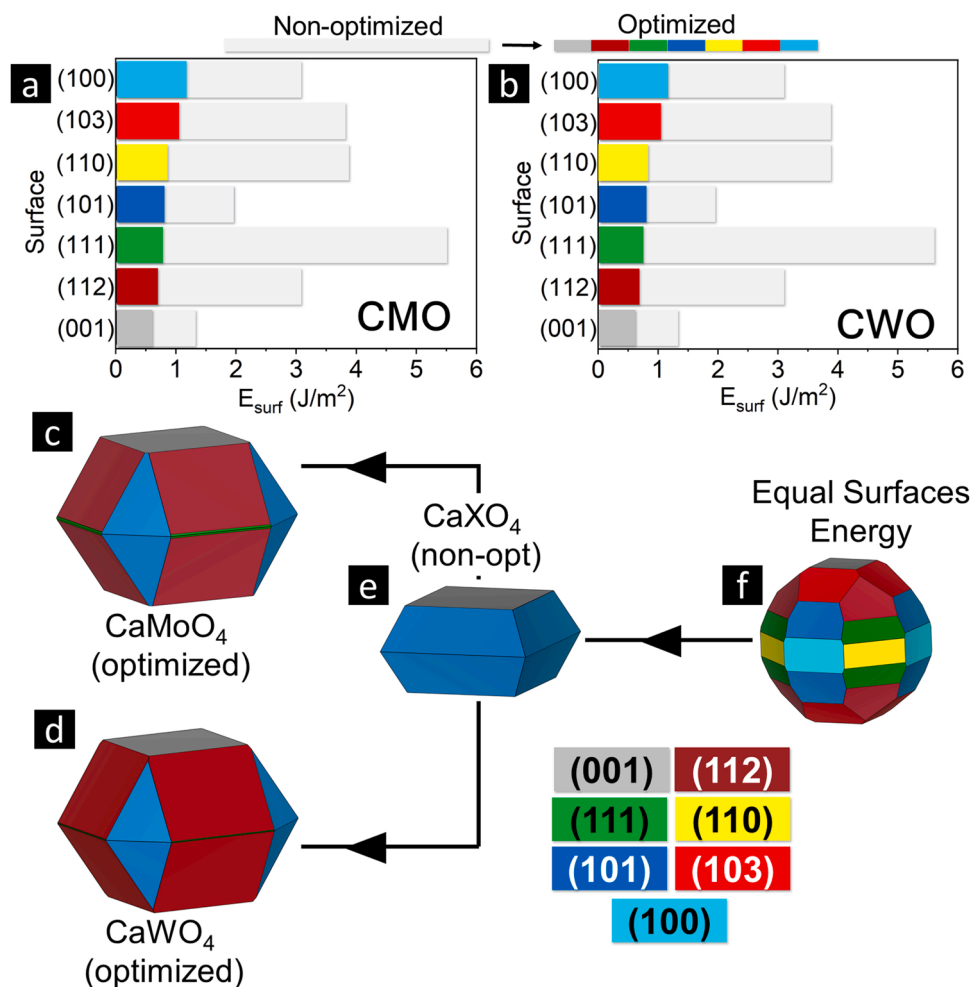|	Surface	E_{surf}	$E_{surf}^{non-opt}$	L	E_{gap}
CaMO$_4$ – CaWO$_4$	(001)	0.61–0.61	0.71–0.71	39.15–39.25	4.39–4.88
	(112)	0.71–0.68	2.36–2.42	18.26–18.24	4.24–4.79
	(111)	0.80–0.77	4.71–4.84	32.66–32.48	4.31–4.88
	(101)	0.82–0.80	1.14–1.15	21.17–21.15	4.46–4.97
	(110)	0.87–0.84	2.98–3.02	26.97–26.77	4.08–4.71
	(103)	1.06–1.04	2.73–2.77	13.45–13.33	4.20–4.80
	(100)	1.19–1.16	1.88–1.92	22.22–22.05	3.45–3.98

Fig. 3. Differences between optimized (colorful bars) and non-optimized (gray bars) indicate the E_{surf} behavior due to the optimization process for (a) CaMoO$_4$ and (b) CaWO$_4$, the morphologies from E_{surf} after optimization for CaMoO$_4$ (c) and CaWO$_4$ (d), respectively, the CaXO$_4$ morphologies of the system generated from non-optimized E_{surf} values (e), and sphere-shaped crystal with equal E_{surf} values for CaXO$_4$ in both systems for visual purposes (f).

surfaces of CaXO$_4$. The outermost layers of the (001) and (112) surfaces (Figs. 2a and 2d, respectively) are composed of [CaO$_6$] and [XO$_4$], and the (100), (101), (103) (110), and (111) surfaces (Figs. 2b, 2c, 2d, 2e, and 2 f) are composed of [CaO$_5$] and [XO$_4$] outermost polyhedra. All outermost Ca-polyhedra have coordination lower than those under the bulk ([CaO$_8$]). On the other hand, the outermost X-centered clusters remain in their original bulk coordination ([XO$_4$]).

Since the surfaces only have terminations with five-fold (5 f) and six-fold (6 f) coordinated Ca-centered polyhedra and four-fold (4 f) coordinated X-centered polyhedra, it is necessary to use a parameter that considers the different geometric distortions of each polyhedra. A parameter that allows the distortion analysis is the effective coordination number (*ECoN*) [74]. *ECoN* is calculated by adding all surrounding atoms of a center through a weighting scheme, with the atoms counted as fractional atoms with values between 0 and 1. This parameter tends to zero according to the increase in the distance of the surrounding atom from the central atom. Therefore, an analysis based on the *ECoN* should consider that for the higher differences between *ECoN* and usual coordination values, the polyhedra will be most distorted. The *ECoN* has been employed in studying diverse compounds with considerable success [75–80].

Concerning the [CaO$_6$] polyhedra, the (112) surface has the highest *ECoN* values, while for [CaO$_5$] polyhedra, the (101), (110), (111) and

the (100) surfaces exhibit the lowest *ECoN*. Regarding the [XO$_4$] polyhedra, the (001) surface has the highest, and the (100) surface has the lowest *ECoN*. The outermost polyhedra are more distorted at the (100) surface, which results in the most unstable surface for CaXO$_4$ (see E_{surf} values in Table 3).

The (101) surface has the lowest density of negative charges indicating its tendency to interact with anionic systems. On the other hand, the (112) surface has the opposite characteristic, i. e., a higher density of negative charges suitable for interacting with cationic systems. All surfaces have similar behavior, with continuous layers of negative charge and islands of positive charge density, except for the (100) surface, which has continuous layers of interspersed negative and positive charge densities. Visually, there are no differences in the electrostatic potential due to the X = Mo or W atom. Therefore, the Hirshfeld atomic charges (*q*) were calculated (Table 2).

Table 2 shows higher charges module (|*q*|) for CaWO$_4$-based systems than for the analogs of CaMoO$_4$. In addition, the bulk has higher |*q*| values for all atoms compared to the surfaces due to the coordination breakdowns generating oxygen vacancies, causing the lowest coordination in the outermost polyhedra, which suggests that the concentration of atom charges is higher in the innermost surface layers. The (103) surface has the highest |*q*| value for outermost O atoms since, in these systems, the atoms are bonded with a single atom with only one close
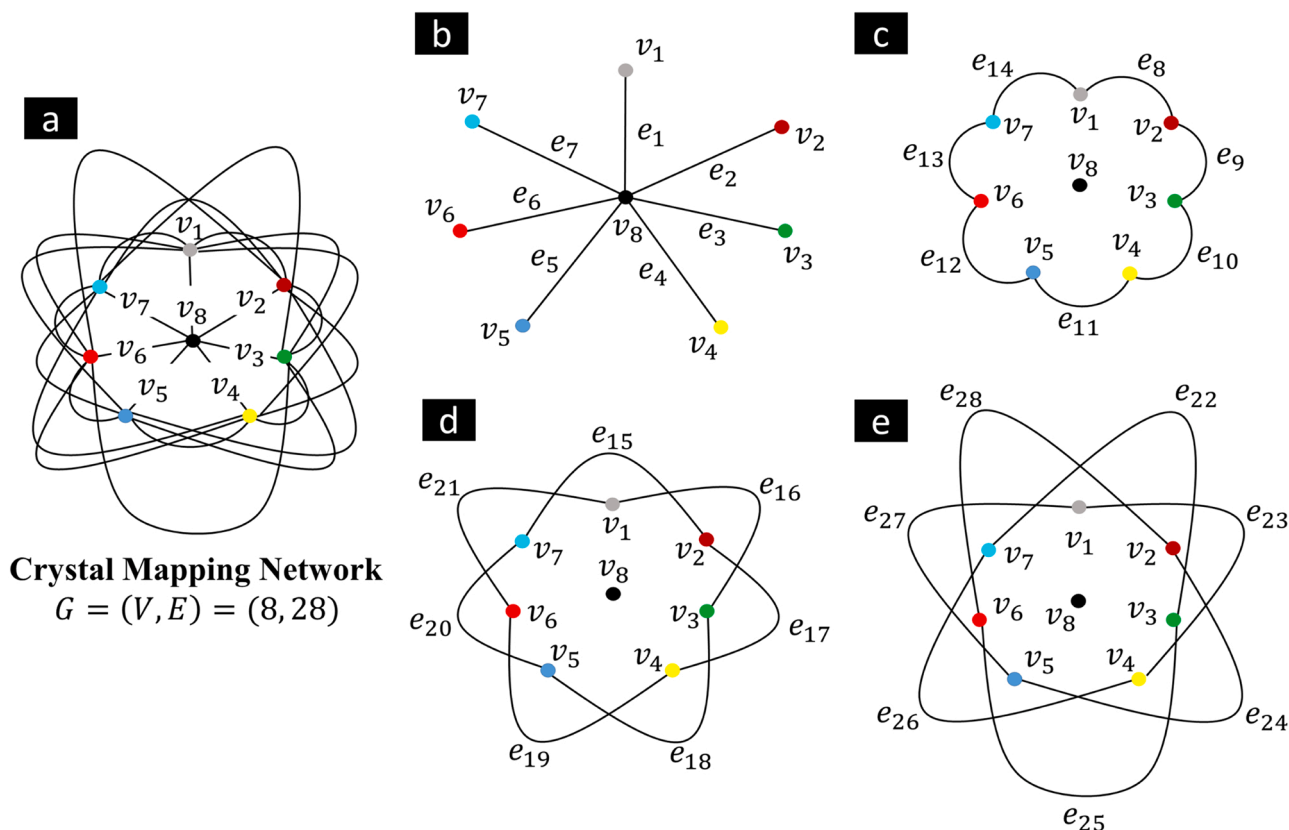
Fig. 4. Diagram of morphologies represented by graph $G = (8, 28)$, in which (a) the seven vertices ($v_1 - v_7$) represent the morphology for which a given (hkl) plane dominates the crystal morphology, and the central apex (v_8) is the thermodynamic crystal. (b) The edges $e_1 - e_7$ are the paths that connect (v_8) to the crystals ($v_1 - v_7$). The paths that connect (c) the next neighbor ($e_8 - e_{14}$), (d) the second neighbor ($e_{15} - e_{21}$), and (e) the third neighbor ($e_{22} - e_{28}$) to the vertices of the crystals are given by the edges that do not pass through the thermodynamic crystal (v_8).

neighbor in the same atomic layer to share the charge.

In the (101) surface, the outermost X atom is localized in an atomic layer below the outermost Ca atomic layer and possesses the highest $|q|$, which corroborates the tendency of such atoms to exhibit a greater $|q|$ in the innermost atomic layers. The highest values of $ECoN$ and $|q|$ were observed for X- and Ca-centered outermost polyhedra in the (101) and (112) surfaces, respectively (Fig. 2), indicating that smaller distortions are associated with greater atomic charges.

Table 3 depicts the surface stability order: (001) > (112) > (111) > (101) > (110) > (103) > (100) for CaXO$_4$. The most similar coordination of Ca-centered polyhedra with respect to the original bulk is responsible for the high relative stability, which can be evidenced by the lower E_{surf} of the (001) and (112) surfaces.

Due to the cutting process are generated oxygen vacancies in the outermost Ca-centered polyhedra, and the outermost atoms rearranged themselves in the optimization process, generating the E_{surf} variations for each (hkl) surface. Considering the E_{surf} values and using Wulff's model, the morphologies associated with the E_{surf} values before and after optimization were determined (Fig. 3).

After structural optimization, it was observed that the (112) surface has the largest exposed area, with a small contribution of (111) for CaMoO$_4$. The only difference between CaMoO$_4$ and CaWO$_4$ is the relative exposure rate of the (111) surface, which is most exposed in CaMoO$_4$. These morphologies (Figs. 3c and 3d) correspond to the ideal system, i. e., without considering the influence of external parameters. Indeed, the influence of surfactants, impurities, solvents, temperature, and synthesis methods, among other factors, can lead to different morphologies.

Therefore, through E_{surf} modulations, one can represent the morphological transformation routes that result in morphologies with maximum relative exposure for each surface, allowing associations between the calculated properties and the experimental data. Thus, it is possible to elaborate a map of the morphological transformations using a graph $G = (V, E, \phi) = (8, 28, 7)$ representation (Fig. 4 and 5).

Instead of using the direct E_{surf} values, this study was based on the surface energy ratio values ($\Gamma_{(hkl)}$), which are given by the expression: $\Gamma_{(hkl)} = E_{surf}^{(hkl)} / E_{surf}^{(001)}$, where $E_{surf}^{(hkl)}$ is the E_{surf} for the index (hkl) surface and $E_{surf}^{(001)}$ is the E_{surf} for the (001) surface, which was chosen as a reference value for being the most stable. It should be mentioned that $\Gamma_{(hkl)}$ is a convenient parameter that shows that the morphology of a particle is given by the ratio between the E_{surf} values.

The Γ values were arranged in matrices for CaMoO$_4$ (Fig. 6a) and CaWO$_4$ (Fig. 6b), where each column corresponds to Γ values for maximum exposure of each (hkl) plane in ascending order of E_{surf}, while the last column shows the Γ values for the ideal morphology.

The morphological route map of the CaMoO$_4$ presented in Fig. 5 can also be used to represent the morphological transformation routes of CaWO$_4$, since these materials have the same symmetry group and relative surface stability order and are only necessary to change the $\Gamma_{(hkl)}$ values (Fig. 7).

These maps can be directly applied to compare and complement experimental results according to NPs morphologies. To this end, the theoretical E_{gap} of two NPs with morphology observed experimentally [41,81] was estimated through the density of states (DOS) weighted by the relative exposure of their exposed surfaces (Fig. 8). In addition, the
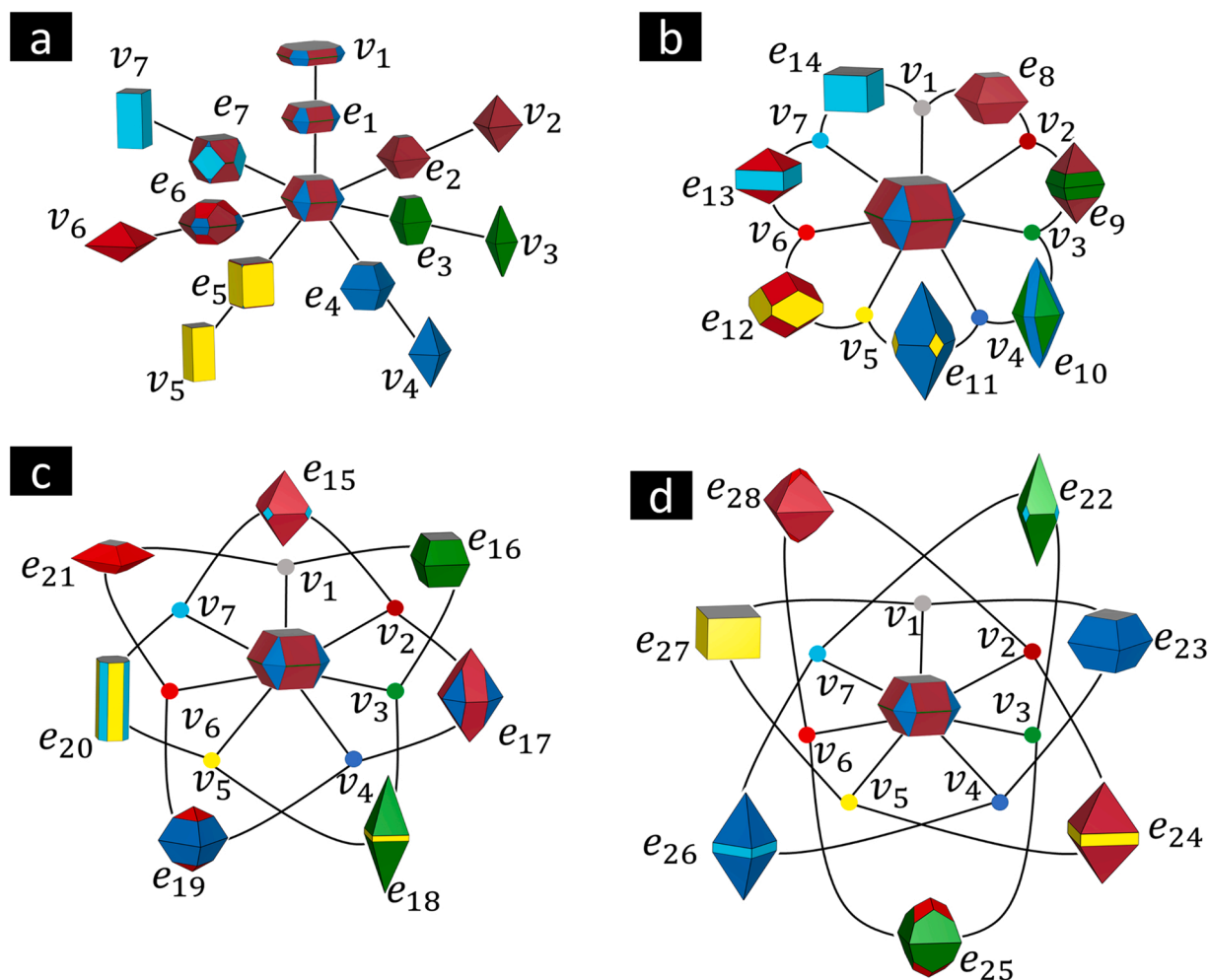
Fig. 5. Morphologies of CaMoO$_4$ crystals associated using surface energy ratio values ($\Gamma_{(hkl)}$). All edges ($e_1 - e_{28}$) provide the energetic pathway to reach the particles located at the vertices ($v_1 - v_8$).

Surface Energy Ratio (Γ^*)

CaMoO$_4$

	v_1	v_2	v_3	v_4	v_5	v_6	v_7	v_8
(001)	0.34	1.00	1.00	1.00	1.00	1.00	1.00	1.00
(112)	1.16	0.34	1.16	1.16	1.16	1.16	1.16	1.16
(111)	1.30	1.30	0.33	1.30	1.30	1.30	1.30	1.30
(110)	1.34	1.34	1.34	0.36	1.34	1.34	1.34	1.34
(101)	1.43	1.43	1.43	1.43	0.33	1.43	1.43	1.43
(103)	1.74	1.74	1.74	1.74	1.74	0.43	1.74	1.74
(100)	1.95	1.95	1.95	1.95	1.95	1.95	0.41	1.95

CaWO$_4$

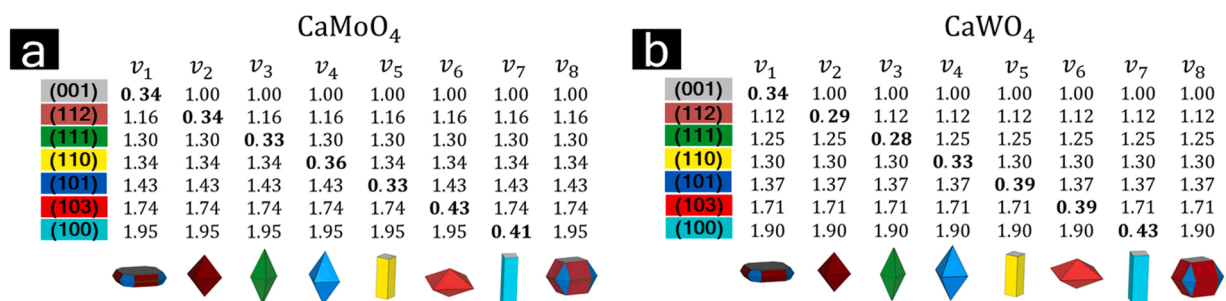|	v_1	v_2	v_3	v_4	v_5	v_6	v_7	v_8
(001)	0.34	1.00	1.00	1.00	1.00	1.00	1.00	1.00
(112)	1.12	0.29	1.12	1.12	1.12	1.12	1.12	1.12
(111)	1.25	1.25	0.28	1.25	1.25	1.25	1.25	1.25
(110)	1.30	1.30	1.30	0.33	1.30	1.30	1.30	1.30
(101)	1.37	1.37	1.37	1.37	0.39	1.37	1.37	1.37
(103)	1.71	1.71	1.71	1.71	1.71	0.39	1.71	1.71
(100)	1.90	1.90	1.90	1.90	1.90	1.90	0.43	1.90

Fig. 6. Surface energy ratios (assuming the energy of the (001) surface as the reference) are used for morphological modulation during vertex determination ($v_1 - v_8$). The image shows the 28 edges that connect the vertices ($e_1 - e_{28}$).

surface exposed in the CaMoO$_4$ synthesized by He et al. [82] was evaluated using a band alignment of surfaces scheme to give information about the photocatalytic activity in acid orange 7 (AO7) degradation (see Fig. 9).

Fig. 8a shows the FEG-SEM micrograph of CaMoO$_4$-oriented nano-octahedra obtained by the microwave-assisted hydrothermal method

at 120 °C for 60 min. In this study, the increase of the microwave time resulted in morphological and E_{gap} changes. For long time intervals, it was not possible to determine a particular morphology because of the agglomeration of the NPs. Fig. 8b displays the micrograph of a nanoparticle with an octahedral morphology. The respective synthesis with β-cyclodextrin-assisted hydrothermal synthesis to prepare 3D flower-
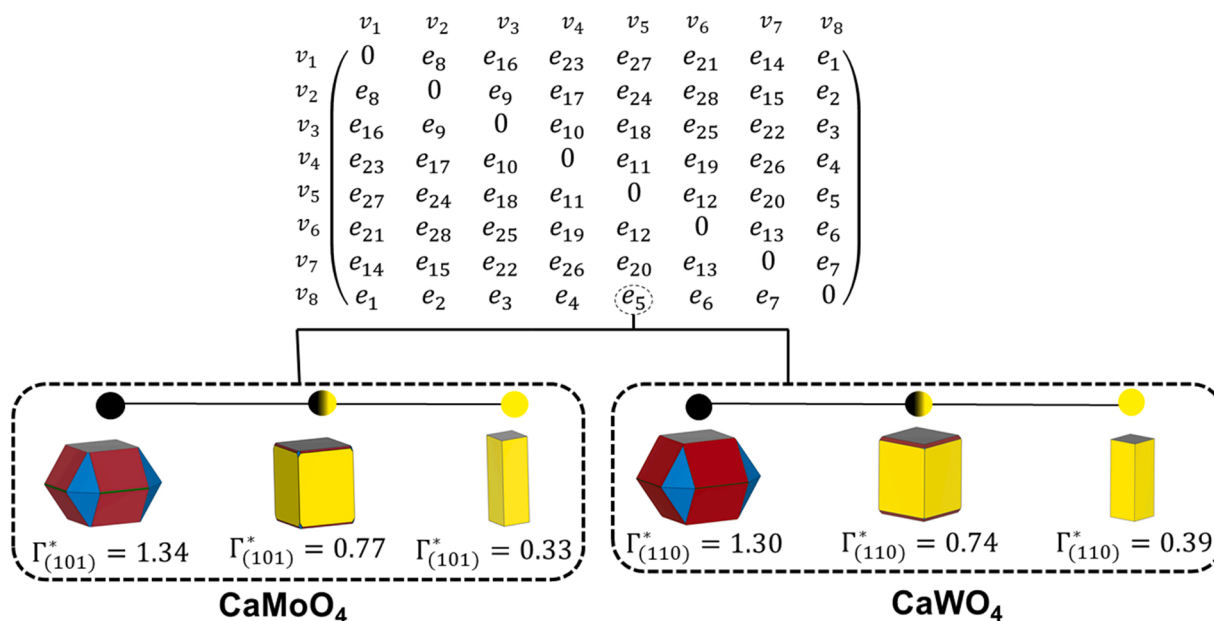
$$
\begin{array}{c}
\begin{array}{cccccccc}
v_1 & v_2 & v_3 & v_4 & v_5 & v_6 & v_7 & v_8
\end{array} \\
\begin{array}{c}
v_1 \\ v_2 \\ v_3 \\ v_4 \\ v_5 \\ v_6 \\ v_7 \\ v_8
\end{array}
\begin{pmatrix}
0 & e_8 & e_{16} & e_{23} & e_{27} & e_{21} & e_{14} & e_1 \\
e_8 & 0 & e_9 & e_{17} & e_{24} & e_{28} & e_{15} & e_2 \\
e_{16} & e_9 & 0 & e_{10} & e_{18} & e_{25} & e_{22} & e_3 \\
e_{23} & e_{17} & e_{10} & 0 & e_{11} & e_{19} & e_{26} & e_4 \\
e_{27} & e_{24} & e_{18} & e_{11} & 0 & e_{12} & e_{20} & e_5 \\
e_{21} & e_{28} & e_{25} & e_{19} & e_{12} & 0 & e_{13} & e_6 \\
e_{14} & e_{15} & e_{22} & e_{26} & e_{20} & e_{13} & 0 & e_7 \\
e_1 & e_2 & e_3 & e_4 & e_5 & e_6 & e_7 & 0
\end{pmatrix}
\end{array}
$$

$\Gamma^*_{(101)} = 1.34$ $\quad$ $\Gamma^*_{(101)} = 0.77$ $\quad$ $\Gamma^*_{(101)} = 0.33$ $\qquad$ $\Gamma^*_{(110)} = 1.30$ $\quad$ $\Gamma^*_{(110)} = 0.74$ $\quad$ $\Gamma^*_{(110)} = 0.39$

CaMoO$_4$ $\qquad\qquad$ **CaWO$_4$**

Fig. 7. The lower triangular matrix represents the adjacent matrix, which was used to illustrate the morphology by changing the energy of a specific surface. For all edges, only the crystal shape at a midpoint is shown.

like CaMoO$_4$ structures self-assembled from octahedral crystals.

Both experimental NPs have similar morphologies, and as it is unknown which surfaces are exposed, two morphologies were proposed according to the modulation of the E_{surf} values. Figs. 8d and 8g shows the modifications made to the E_{surf} value to obtain the proposed morphologies. The first morphology (Fig. 8c) has (101) and (111) exposed surfaces and an E_{gap} of 2.92 eV, which was determined by the sum of the weighted DOS. Similar to the first morphology, the second morphology (Fig. 8f) has (101) and (112) exposed planes and an E_{gap} of 2.80 eV.

He et al. [82] prepared CaMoO$_4$ by the hydrothermal method using different pH values of synthesis, a fact that can influence the morphology of crystals, and evaluated the sonocatalytic performance of each synthesized system in the removal of AO7 [83,84]. According to the results, at pH = 7, the microspheres showed superior sonocatalytic performance, which is attributed to the generation of hydroxyl radicals ($\bullet OH$), superoxide anion radicals ($^{\bullet}O_2-$) and holes (h^+). Observing the micrographs referring to CaMoO$_4$-7, it is not possible to visualize a well-defined morphology, although there are some octahedral shapes in the agglomerate nanoparticle.

Based on the methodology proposed by Toroker et al. [85], to evaluate band edge positions in potential transition metal oxides, the band alignment was built for the CaXO$_4$ surfaces. According to this methodology, the positions of the conduction band minimum (E_{CBM}) and the valence band maximum (E_{VBM}) are defined by $E_{CBM/VBM} = E_{BGC} \pm 0.5E_{gap} - E_e$, where E_{BGC} is the energy of the band gap center, and E_e is the normal hydrogen electrode (NHE) potential (4.5eV). To evaluate the applicability of the systems studied for photocatalysis, four dashed lines representing the E^0, $E^0(O_2/H_2O)$, E^0 and E^0 redox potentials are introduced in Fig. 9.

As observed in Fig. 9, all CaMoO$_4$ surfaces have photocatalytic potential for AO7 removal except for (101). He et al. [82] analyzed the XRD data and showed a peak associated with the (112) surface, which in its energetic stabilization for this surface generates octahedral shapes (v_2 in Fig. 5a) and exhibits band alignment conditions for the degradation mechanism.

4. Conclusions

The same surface stability order of the studied systems and other similar characteristics can be explained by the fact that the lattice-forming atoms (Mo and W) have very similar properties, confirming that, among scheelite-type ABO$_4$ molybdates or tungstates, the stability of the surfaces is determined by the A^{2+} cation. It was also demonstrated that the complete acknowledgment of surface terminations and their electronic and structural properties could provide a basis to estimate phenomena and the types of interactions that can occur in the experimental environment. Furthermore, the results show that almost all surfaces of both systems have band alignment propitious for the occurrence of important mechanisms in photocatalytic environmental remediation.

Using the ideal morphology as a starting point and performing variations in the E_{surf} values, a complete map of morphological transformations of CaXO$_4$ compounds was proposed. These results can be used to understand morphological transformations, growth control, and photocatalysis mechanisms based on DFT simulations. Such information can be very useful to experimentalists to analyze and discuss results obtained by scanning electron microscopy and transmission electron microscopy.

Declaration of Competing Interest

The authors declare that they have no known competing financial interests or personal relationships that could have appeared to influence the work reported in this paper.

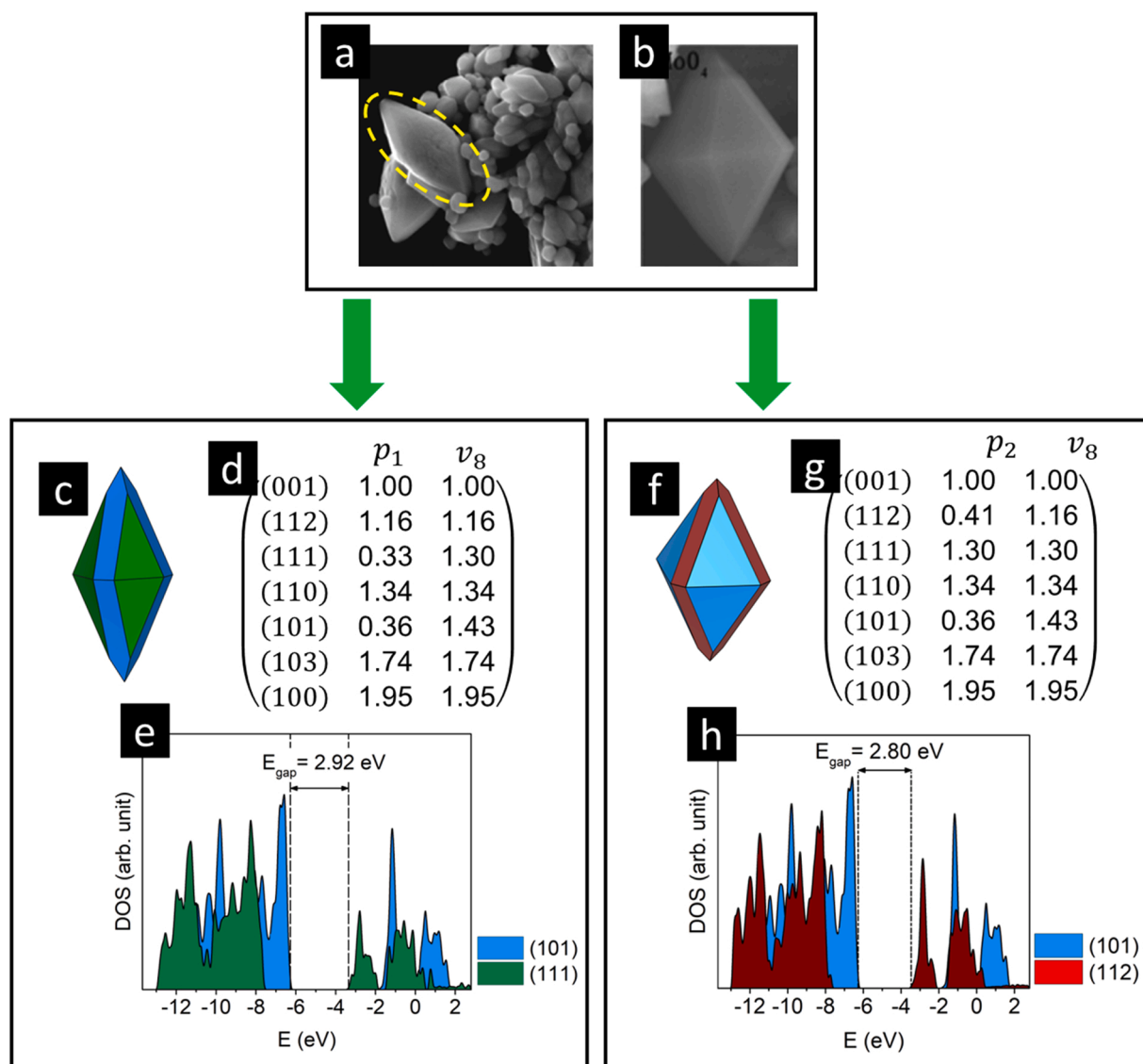### Data Availability

Data will be made available on request.

Fig. 8. (a) FEG-SEM micrograph of CaMoO$_4$-oriented nano-octahedra obtained by the microwave-assisted hydrothermal method at 120 °C for 60 min. Copyright 2011 American Chemical Society; and (b) nanoparticle obtained by β-cyclodextrin-assisted hydrothermal synthesis used for preparing 3D flower-like CaMoO$_4$ structures, which are self-assembled from octahedral crystals. On the left: (c) particle built from the Wulff model showing the exposed (101) and (111) surfaces, (d) their respective energy modulations, and (e) an estimate of its E_{gap} through the density of states weighted by the percentage of the exposed area on each surface. On the right: (f) another Wulff particle that corresponds to the morphologies observed experimentally highlighting their exposed (101) and (112) surfaces, (g) their respective energy modulations, and (h) E_{gap} through the density of states weighted by the percentage of the exposed area of each surface. Adapted with permission from ref [41].
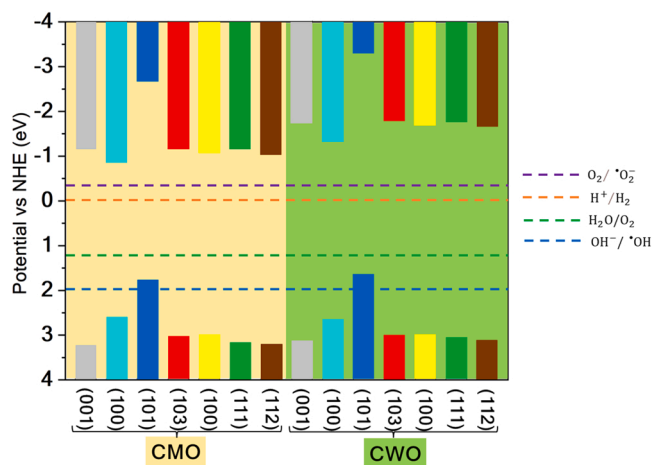
Fig. 9. Band alignment for CaMoO$_4$ (CMO) and CaWO$_4$ (CWO) surfaces.

Acknowledgments

References

[1] E.A. Tsiwah, Y. Ding, Z. Li, Z. Zhao, M. Wang, C. Hu, X. Liu, C. Sun, X. Zhao, Y. Xie, One-pot scalable synthesis of all-inorganic perovskite nanocrystals with tunable morphology, composition and photoluminescence, CrystEngComm 19 (2017) 7041–7049, https://doi.org/10.1039/C7CE01749A.

[2] M.C. Oliveira, L. Gracia, I.C. Nogueira, M.F.C. Gurgel, J.M.R. Mercury, E. Longo, J. Andrés, On the morphology of BaMoO4 crystals: a theoretical and experimental

approach, Cryst. Res. Technol. 51 (2016) 634–644, https://doi.org/10.1002/crat.201600227.

[3] Y.K. Ren, X.H. Ding, Y.H. Wu, J. Zhu, T. Hayat, A. Alsaedi, Y.F. Xu, Z.Q. Li, S. F. Yang, S.Y. Dai, Temperature-assisted rapid nucleation: a facile method to optimize the film morphology for perovskite solar cells, J. Mater. Chem. A 5 (2017) 20327–20333, https://doi.org/10.1039/c7ta06334b.

[4] J.A.S. Laranjeira, G.S.L. Fabris, M.M. Ferrer, A.R. Albuquerque, J.R. Sambrano, Morphological transformation network of nanoparticles via DFT simulations, Cryst. Growth Des. 20 (2020) 4600–4611, https://doi.org/10.1021/acs.cgd.0c00423.

[5] Q. Liang, F. Qiao, X. Cui, X. Hou, Controlling the morphology of ZnO structures via low temperature hydrothermal method and their optoelectronic application, Mater. Sci. Semicond. Process. 89 (2019) 154–160, https://doi.org/10.1016/j.mssp.2018.09.007.

[6] N.F. Andrade Neto, P.M. Oliveira, M.R.D. Bomio, F.V. Motta, Effect of temperature on the morphology and optical properties of Ag2WO4 obtained by the co-precipitation method: photocatalytic activity, Ceram. Int. 45 (2019) 15205–15212, https://doi.org/10.1016/j.ceramint.2019.05.006.

[7] W. Wu, J. Wang, T. Zhang, S. Jiang, X. Ma, G. Zhang, X. Zhang, X. Chen, B. Li, Controllable synthesis of Ag/AgCl@MIL-88A: Via in situ growth method for morphology-dependent photocatalytic performance, J. Mater. Chem. C. 7 (2019) 5451–5460, https://doi.org/10.1039/c9tc00398c.

[8] M. Li, Y. Yang, Y. Ling, W. Qiu, F. Wang, T. Liu, Y. Song, X. Liu, P. Fang, Y. Tong, Y. Li, Morphology and doping engineering of Sn-doped hematite nanowire photoanodes, Nano Lett. 17 (2017) 2490–2495, https://doi.org/10.1021/acs.nanolett.7b00184.

[9] O. Almamoun, S.Y. Ma, Effect of Mn doping on the structural, morphological and optical properties of SnO2 nanoparticles prepared by Sol-gel method, Mater. Lett. 199 (2017) 172–175, https://doi.org/10.1016/j.matlet.2017.04.075.

[10] B.G. Alamani, J.D. Gale, J.D. Rimer, Zinc ions modify calcium oxalate growth by distinct transformation of crystal surface termination, Cryst. Growth Des. 21 (2021) 3375–3383, https://doi.org/10.1021/acs.CGD.1C00016.

[11] L.H.S. Lacerda, M.A. San-Miguel, S.R. de Lazaro, Surface and morphological studies of LiNbO 3: p-type semiconductivity on stoichiometric surfaces, New J. Chem. 45 (2021) 16594–16605, https://doi.org/10.1039/D1NJ02429A.

[12] Z. Yan, W. Xue, D. Mei, Density functional theory study on the morphology evolution of hydroxylated β-cristobalite silica and desilication in the presence of methanol, J. Phys. Chem. C 125 (2021) 7868–7879, https://doi.org/10.1021/ACS.JPCC.0C11368.

[13] X. Tian, P. Li, T. Wang, Morphology of MoP catalyst under hydrogenation conditions: a DFT based thermodynamics study, Mol. Catal. 464 (2019) 57–62, https://doi.org/10.1016/J.MCAT.2018.12.010.

[14] L. Cheng, X. Yu, J. Zhang, W. Li, C. Zhao, Z. Wang, L. Jin, DFT investigations into surface stability and morphology of δ-MoC catalyst, Appl. Surf. Sci. 497 (2019), 143790, https://doi.org/10.1016/J.APSUSC.2019.143790.

[15] M. Zhang, W. Wang, Y. Chen, Insight of DFT and ab initio atomistic thermodynamics on the surface stability and morphology of In2O3, Appl. Surf. Sci. 434 (2018) 1344–1352, https://doi.org/10.1016/J.APSUSC.2017.11.258.

[16] A. Piovano, M. D'Amore, T. Wada, P. Cleto Bruzzese, G. Takasao, A. Thakur, P. Chammingkwan, M. Terano, B. Civalleri, S. Bordiga, T. Taniike, E. Groppo, Revisiting the identity of δ-MgCl2: part II. Morphology and exposed surfaces studied by vibrational spectroscopies and DFT calculation, J. Catal. 387 (2020) 1–11, https://doi.org/10.1016/J.JCAT.2020.04.017.

[17] R.A.P. Ribeiro, M.C. Oliveira, M.R.D. Bomio, S.R. de Lazaro, J. Andrés, E. Longo, Connecting the surface structure, morphology and photocatalytic activity of Ag2O: an in depth and unified theoretical investigation, Appl. Surf. Sci. 509 (2020), 145321, https://doi.org/10.1016/J.APSUSC.2020.145321.

[18] A.F. Gouveia, L. Gracia, E. Longo, M.A. San-Miguel, J. Andrés, Modulating the properties of multifunctional semiconductors by means of morphology: theory meets experiments, Comput. Mater. Sci. 188 (2021), 110217, https://doi.org/10.1016/J.COMMATSCI.2020.110217.

[19] V. Teodoro, A.F. Gouveia, T.R. Machado, A.B. Trench, N. Jacomaci, M. Assis, G. E. Marques, M.D. Teodoro, M.A. San-Miguel, J. Andrés, J. Bettini, E. Longo, Connecting morphology and photoluminescence emissions in β-Ag2MoO4 microcrystals, Ceram. Int. 48 (2022) 3740–3750, https://doi.org/10.1016/J.CERAMINT.2021.10.156.

[20] L.H. da, S. Lacerda, M.A. San-Miguel, DFT approaches unraveling the surface and morphological properties of MnMoO4, Appl. Surf. Sci. 567 (2021), 150882, https://doi.org/10.1016/J.APSUSC.2021.150882.

[21] G. Wulff, XXV. Zur frage der geschwindigkeit des wachsthums und der auflösung der krystallflächen, Z. Krist. Cryst. Mater. 34 (1901), https://doi.org/10.1524/zkri.1901.34.1.449.

[22] F. Zhu, Z. Xiao, F. Zhang, L. Yan, A. Huang, Donor doping process and white light generation in CaMoO4 powders with multivalence Pr codoping, J. Lumin. 131 (2011) 22–24, https://doi.org/10.1016/J.JLUMIN.2010.08.019.

[23] L.L. Nagornaya, F.A. Danevich, A.M. Dubovik, B.V. Grinyov, S. Henry, V. Kapustyanyk, H. Kraus, D.V. Poda, V.M. Kudovbenko, V.B. Mikhailik, M. Panasyuk, O.G. Polischuk, V. Rudyk, V. Tsybulskyi, I.A. Tupitsyna, Y. Y. Vostretsov, Tungstate and molybdate scintillators to search for dark matter and double beta decay, IEEE Trans. Nucl. Sci. 56 (2009) 2513–2518, https://doi.org/10.1109/TNS.2009.2022268.

[24] A.M. Kaczmarek, R. van Deun, Rare earth tungstate and molybdate compounds – from 0D to 3D architectures, Chem. Soc. Rev. 42 (2013) 8835–8848, https://doi.org/10.1039/C3CS60166H.

[25] W. Eerenstein, N.D. Mathur, J.F. Scott, Multiferroic and magnetoelectric materials, Nature 2006 442:7104. 442 (2006) 759–765. https://doi.org/10.1038/nature05023.

[26] H. Wiegelmann, B.K. Ponomarev, J. van Tol, A.G.M. Jansen, P. Wyder, B. S. Red'kin, Magnetoelectric properties of ferroelectric rare earth molybdates, Ferroelectrics 183 (2011) 195–204, https://doi.org/10.1080/00150199608224106.

[27] T.A. Blank, L.P. Eksperiandova, K.N. Belikov, Recent trends of ceramic humidity sensors development: a review, Sens. Actuators B Chem. 228 (2016) 416–442, https://doi.org/10.1016/J.SNB.2016.01.015.

[28] M.V. Arularasu, R. Sundaram, C.M. Magdalane, K. Kanimozhi, K. Kasinathan, F. T. Thema, D. Letsholathebe, G.T. Mola, M. Maaza, Synthesis, humidity sensing, photocatalytic and antimicrobial properties of thin film nanoporous PbWO4-WO3 nanocomposites, J. Nanostruct. 7 (2017) 47–56, https://doi.org/10.22052/JNS.2017.01.006.

[29] W. Gulbinski, T. Suszko, W. Sienicki, B. Warcholiński, Tribological properties of silver- and copper-doped transition metal oxide coatings, Wear 254 (2003) 129–135, https://doi.org/10.1016/S0043-1648(02)00292-2.

[30] W.D. Robertson, Molybdate and tungstate as corrosion inhibitors and the mechanism of inhibition, J. Electrochem. Soc. 98 (1951) 94, https://doi.org/10.1149/1.2778118.

[31] M.S. Vukasovich, J.P.G. Farr, Molybdate in corrosion inhibition—a review, Polyhedron 5 (1986) 551–559, https://doi.org/10.1016/S0277-5387(00)84963-3.

[32] J. Sottmann, M. Herrmann, P. Vajeeston, A. Ruud, C. Drathen, H. Emerich, D. S. Wragg, H. Fjellvåg, Bismuth vanadate and molybdate: stable alloying anodes for sodium-ion batteries, Chem. Mater. 29 (2017) 2803–2810, https://doi.org/10.1021/ACS.CHEMMATER.6B04699.

[33] H.-H. Xi, D. Zhou, H.-D. Xie, B. He, Q.-P. Wang, Raman spectrad, infrared spectra, and microwave dielectric properties of low-temperature firing [(Li0.5Ln0.5) 1−xCax]MoO4 (Ln = Sm and Nd) solid solution ceramics with scheelite structure, J. Am. Ceram. Soc. 98 (2015) 587–593, https://doi.org/10.1111/JACE.13332.

[34] C. Li, G. Chen, J. Sun, J. Rao, Z. Han, Y. Hu, Y. Zhou, A novel mesoporous single-Crystal-Like Bi2WO6 with enhanced photocatalytic activity for pollutants degradation and oxygen production, ACS Appl. Mater. Interfaces 7 (2015) 25716–25724, https://doi.org/10.1021/ACSAMI.5B06995.

[35] M. Ratova, G.T. West, P.J. Kelly, Photocatalytic visible-light active bismuth tungstate coatings deposited by reactive magnetron sputtering, Vacuum 115 (2015) 66–69, https://doi.org/10.1016/J.VACUUM.2015.02.003.

[36] J. Liu, Y. Liu, C. Li, X. Wang, H. Gao, Z. Liu, W. Chen, Green upconversion emissions in Er3+/Yb3+ co-doped CaMoO4 prepared by microwave-assisted metathetic method, J. Nanosci. Nanotechnol. 16 (2016) 802–806, https://doi.org/10.1166/JNN.2016.10810.

[37] N. Zhang, W. Bu, Y. Xu, D. Jiang, J. Shi, Self-assembled flowerlike europium-doped lanthanide molybdate microarchitectures and their photoluminescence properties, J. Phys. Chem. C. 111 (2007) 5014–5019, https://doi.org/10.1021/JP064624O.

[38] J. Liu, A.M. Kaczmarek, J. Billet, I. van Driessche, R. van Deun, Upconversion luminescence of lanthanide-doped mixed CaMoO4–CaWO4 micro-/nano-materials, Dalton Trans. 45 (2016) 12094–12102, https://doi.org/10.1039/C6DT01555G.

[39] M.R.D. Bomio, R.L. Tranquilin, F.V. Motta, C.A. Paskocimas, R.M. Nascimento, L. Gracia, J. Andres, E. Longo, , Toward understanding the photocatalytic activity of PbMoO 4 powders with predominant (111), (100), (011), and (110) facets. A combined experimental and theoretical study, J. Phys. Chem. C. (2013), https://doi.org/10.1021/jp407416h.

[40] F.K.F. Oliveira, M.C. Oliveira, L. Gracia, R.L. Tranquilin, C.A. Paskocimas, F. V. Motta, E. Longo, J. Andrés, Experimental and theoretical study to explain the morphology of CaMoO 4 crystals, J. Phys. Chem. Solids 114 (2018) 141–152, https://doi.org/10.1016/j.jpcs.2017.11.019.

[41] V.M. Longo, L.S. Cavalcante, E.C. Paris, J.C. Sczancoski, P.S. Pizani, M.S. Li, J. Andrés, E. Longo, J.A. Varela, Hierarchical assembly of CaMoO4nano-octahedrons and their photoluminescence properties, J. Phys. Chem. C 115 (2011) 5207–5219, https://doi.org/10.1021/JP1082328.

[42] V.M. Longo, L. Gracia, D.G. Stroppa, L.S. Cavalcante, M. Orlandi, A.J. Ramirez, E. R. Leite, J. Andrés, A. Beltrán, J.A. Varela, E. Longo, A joint experimental and theoretical study on the nanomorphology of CaWO 4 crystals, J. Phys. Chem. C 115 (2011) 20113–20119, https://doi.org/10.1021/jp205764s.

[43] M.M. Ferrer, G.S.L. Fabris, B.V. de Faria, J.B.L. Martins, M.L. Moreira, J. R. Sambrano, Quantitative evaluation of the surface stability and morphological changes of Cu2O particles, Heliyon 5 (2019), https://doi.org/10.1016/j.heliyon.2019.e02500.

[44] A.F. Gouveia, M.M. Ferrer, J.R. Sambrano, J. Andrés, E. Longo, Modeling the atomic-scale structure, stability, and morphological transformations in the tetragonal phase of LaVO4, Chem. Phys. Lett. 660 (2016) 87–92, https://doi.org/10.1016/j.cplett.2016.08.013.

[45] M.A. Barbosa, G.S.L. Fabris, M.M. Ferrer, D.H.M. Azevedo, J.R. Sambrano, Computational simulations of morphological transformations by surface structures: the case of rutile TiO2 phase, Mater. Res. 20 (2017) 920–925, https://doi.org/10.1590/1980-5373-MR-2016-0709.

[46] L. Yu, D. Li, M. Yue, J. Yao, S. Lu, Dependence of morphology and photoluminescent properties of GdPO4:Eu3+ nanostructures on synthesis condition, Chem. Phys. 326 (2006) 478–482, https://doi.org/10.1016/j.chemphys.2006.03.008.

[47] X.M. Lin, C.M. Sorensen, K.J. Klabunde, G.C. Hadjipanayis, Temperature dependence of morphology and magnetic properties of cobalt nanoparticles prepared by an inverse micelle technique, Langmuir 14 (1998) 7140–7146, https://doi.org/10.1021/la980509w.

[48] T. Ohgaki, N. Ohashi, H. Kakemoto, S. Wada, Y. Adachi, H. Haneda, T. Tsurumi, Growth condition dependence of morphology and electric properties of ZnO films on sapphire substrates prepared by molecular beam epitaxy, J. Appl. Phys. 93 (2003) 1961–1965, https://doi.org/10.1063/1.1535256.

[49] M. Kusuma, G.T. Chandrappa, Effect of calcination temperature on characteristic properties of CaMoO 4 nanoparticles, J. Sci.: Adv. Mater. Devices 4 (2019) 150–157, https://doi.org/10.1016/j.jsamd.2019.02.003.

[50] J. Bhagwan, S.K. Hussain, J.S. Yu, Facile hydrothermal synthesis and electrochemical properties of CaMoO4 nanoparticles for aqueous asymmetric supercapacitors, ACS Sustain. Chem. Eng. 7 (2019) 12340–12350, https://doi.org/10.1021/acssuschemeng.9b01708.

[51] P.Y. He, Y.J. Zhang, H. Chen, L.C. Liu, Development of an eco-efficient CaMoO4/electroconductive geopolymer composite for recycling silicomanganese slag and degradation of dye wastewater, J. Clean. Prod. 208 (2019) 1476–1487, https://doi.org/10.1016/j.jclepro.2018.10.176.

[52] S. Wang, H. Gao, G. Sun, Y. Li, Y. Wang, H. Liu, C. Chen, Liang Yang, Structure characterization, optical and photoluminescence properties of scheelite-type CaWO4 nanophosphors: effects of calcination temperature and carbon skeleton, Opt. Mater. (Amst.) 99 (2020), 109562, https://doi.org/10.1016/J.OPTMAT.2019.109562.

[53] F. Akman, M.R. Kaçal, N. Almousa, M.I. Sayyed, H. Polat, Gamma-ray attenuation parameters for polymer composites reinforced with BaTiO3 and CaWO4 compounds, Prog. Nucl. Energy 121 (2020), 103257, https://doi.org/10.1016/j.pnucene.2020.103257.

[54] W. Xu, Y. Cui, Y. Hu, L. Zheng, Z. Zhang, W. Cao, Optical temperature sensing in Er3+-Yb3+ codoped CaWO4 and the laser induced heating effect on the luminescence intensity saturation, J. Alloy. Compd. 726 (2017) 547–555, https://doi.org/10.1016/j.jallcom.2017.08.007.

[55] P. Hohenberg, W. Kohn, Inhomogeneous electron gas, Phys. Rev. 136 (1964) B864, https://doi.org/10.1103/PHYSREV.136.B864.

[56] H. David, J. Donnay, A new law of crystal morphology extending the Law of Bravais, 22 (1937) 446–467.

[57] P. Hartman, W.G. Perdok, On the relations between structure and morphology of crystals. I, Acta Crystallogr. 8 (1955) 49–52, https://doi.org/10.1107/s0365110x55000121.

[58] J. Prywer, Explanation of some peculiarities of crystal morphology deduced from the BFDH law, J. Cryst. Growth 270 (2004) 699–710, https://doi.org/10.1016/j.jcrysgro.2004.06.046.

[59] R. Dovesi, A. Erba, R. Orlando, C.M. Zicovich-Wilson, B. Civalleri, L. Maschio, M. Rérat, S. Casassa, J. Baima, S. Salustro, B. Kirtman, Quantum-mechanical condensed matter simulations with CRYSTAL, Wiley Interdiscip. Rev. Comput. Mol. Sci. 8 (2018), e1360, https://doi.org/10.1002/wcms.1360.

[60] M.F. Peintinger, D.V. Oliveira, T. Bredow, Consistent Gaussian basis sets of triple-zeta valence with polarization quality for solid-state calculations, J. Comput. Chem. 34 (2013) 451–459, https://doi.org/10.1002/JCC.23153.

[61] F. Corà, An ab initio Hartree-Fock study of α-MoO3, J. Mater. Chem. 7 (1997) 959–967, https://doi.org/10.1039/a607439a.

[62] F. Corà, A. Patel, N.M. Harrison, R. Dovesi, C.R.A. Callow, An ab initio Hartree-Fock study of the cubic and tetragonal phases of bulk tungsten trioxide, J. Am. Chem. Soc. 118 (1996) 12174–12182, https://doi.org/10.1021/ja961514u.

[63] T. Bredow, K. Jug, R.A. Evarestov, Electronic and magnetic structure of ScMnO3, Phys. Status Solidi (b) 243 (2006) R10–R12, https://doi.org/10.1002/PSSB.200541403.

[64] F.A. Rabuffetti, S.P. Culver, L. Suescun, R.L. Brutchey, Structural disorder in AMoO4 (A = Ca, Sr, Ba) scheelite nanocrystals, Inorg. Chem. 53 (2014) 1056–1061, https://doi.org/10.1021/ic4025348.

[65] D.I. Bilc, R. Orlando, R. Shaltaf, G.M. Rignanese, J. Íñiguez, P. Ghosez, Hybrid exchange-correlation functional for accurate prediction of the electronic and structural properties of ferroelectric oxides, Phys. Rev. B Condens. Matter Mater. Phys. 77 (2008), 165107 https://doi.org/10.1103.

[66] A.D. Becke, Density-functional thermochemistry. IV. A new dynamical correlation functional and implications for exact-exchange mixing, J. Chem. Phys. 104 (1998) 1040, https://doi.org/10.1063/1.470829.

[67] A.V. Krukau, O.A. Vydrov, A.F. Izmaylov, G.E. Scuseria, Influence of the exchange screening parameter on the performance of screened hybrid functionals, J. Chem. Phys. 125 (2006), 224106, https://doi.org/10.1063/1.2404663.

[68] J.P. Perdew, K. Burke, M. Ernzerhof, Generalized gradient approximation made simple, Phys. Rev. Lett. 77 (1996) 3865, https://doi.org/10.1103/PhysRevLett.77.3865.

[69] C. Adamo, V. Barone, Toward reliable density functional methods without adjustable parameters: the PBE0 model, J. Chem. Phys. 110 (1999) 6158, https://doi.org/10.1063/1.478522.

[70] R. Demichelis, B. Civalleri, M. Ferrabone, R. Dovesi, On the performance of eleven DFT functionals in the description of the vibrational properties of aluminosilicates, Int. J. Quantum Chem. 110 (2010) 406–415, https://doi.org/10.1002/QUA.22301.

[71] E.O. Gomes, G.S.L. Fabris, M.M. Ferrer, F.V. Motta, M.R.D. Bomio, J. Andres, E. Longo, J.R. Sambrano, Computational procedure to an accurate DFT simulation to solid state systems, Comput. Mater. Sci. 170 (2019), 109176, https://doi.org/10.1016/j.commatsci.2019.109176.

[72] V.V. Bakovets, I.V. Yushina, O.V. Antonova, E.S. Zolotova, Bandgap-width correction for luminophores CaMoO4 and CaWO4, Optics and Spectroscopy 2017 123:3. 123 (2017) 399–403. https://doi.org/10.1134/S0030400X17090053.

[73] A. Zalkin, D.H. Templeton, X-ray diffraction refinement of the calcium tungstate structure, J. Chem. Phys. 40 (1964) 501–504, https://doi.org/10.1063/1.1725143.

[74] K. Momma, F. Izumi, VESTA: a three-dimensional visualization system for electronic and structural analysis, Urn:Issn:0021-8898 41 (2008) 653–658, https://doi.org/10.1107/S0021889808012016.

[75] J.L.F. da Silva, Effective coordination concept applied for phase change (GeTe)m (Sb2Te3)n compounds, J. Appl. Phys. 109 (2011), 023502, https://doi.org/10.1063/1.3533422.

[76] A. Romanchuk, A. Trigub, T. Plakhova, A. Kuzenkova, R. Svetogorov, K. Kvashnina, S. Kalmykov, Effective coordination numbers from EXAFS: general approaches for lanthanide and actinide dioxides, J. Synchrotron Radiat. 29 (2022) 288–294, https://doi.org/10.1107/S160057752101300X.

[77] M.Attarian Shandiz, Effective coordination number model for the size dependency of physical properties of nanocrystals, J. Phys.: Condens. Matter 20 (2008), 325237, https://doi.org/10.1088/0953-8984/20/32/325237.

[78] M.J. Piotrowski, P. Piquini, J.L.F. da Silva, Density functional theory investigation of 3d, 4d, and 5d 13-atom metal clusters, Phys. Rev. B Condens. Matter Mater. Phys. 81 (2010), 155446, https://doi.org/10.1103/PHYSREVB.81.155446.

[79] F.P. Sabino, L.N. Oliveira, S.H. Wei, J.L.F. da Silva, Tuning the optical bandgap in multi-cation compound transparent conducting-oxides: the examples of In2ZnO4 and In4Sn3O12, J. Appl. Phys. 123 (2018), 055704, https://doi.org/10.1063/1.5018056.

[80] J.E. Medvedeva, I.A. Zhuravlev, C. Burris, D.B. Buchholz, M. Grayson, R.P. H. Chang, Origin of high carrier concentration in amorphous wide-bandgap oxides: role of disorder in defect formation and electron localization in In2O3−x, J. Appl. Phys. 127 (2020), 175701, https://doi.org/10.1063/1.5144219.

[81] X. Liu, L. Li, H.M. Noh, S.H. Park, J.H. Jeong, H.K. Yang, K. Jang, D.S. Shin, Synthesis and photoluminescence of novel 3D flower-like CaMoO4 architectures hierarchically self-assembled with tetragonal bipyramid nanocrystals, Opt. Mater. 43 (2015) 10–17, https://doi.org/10.1016/J.OPTMAT.2015.02.014.

[82] L.L. He, Y. Zhu, Q. Qi, X.Y. Li, J.Y. Bai, Z. Xiang, X. Wang, Synthesis of CaMoO4 microspheres with enhanced sonocatalytic performance for the removal of Acid Orange 7 in the aqueous environment, Sep. Purif. Technol. 276 (2021), 119370, https://doi.org/10.1016/J.SEPPUR.2021.119370.

[83] C. Qi, X. Liu, J. Ma, C. Lin, X. Li, H. Zhang, Activation of peroxymonosulfate by base: implications for the degradation of organic pollutants, Chemosphere 151 (2016) 280–288, https://doi.org/10.1016/J.CHEMOSPHERE.2016.02.089.

[84] T.X.H. Le, R. Esmilaire, M. Drobek, M. Bechelany, C. Vallicari, S. Cerneaux, A. Julbe, M. Cretin, Nitrogen-doped graphitized carbon electrodes for biorefractory pollutant removal, J. Phys. Chem. C 121 (2017) 15188–15197, https://doi.org/10.1021/ACS.JPCC.7B03100.

[85] M.C. Toroker, D.K. Kanan, N. Alidoust, L.Y. Isseroff, P. Liao, E.A. Carter, First principles scheme to evaluate band edge positions in potential transition metal oxide photocatalysts and photoelectrodes, Phys. Chem. Chem. Phys. 13 (2011) 16644–16654, https://doi.org/10.1039/C1CP22128K.